Available online at www.sciencedirect.com
ScienceDirect
Trans. Nonferrous Met. Soc. China 33(2023) 438−453
Transactions of Nonferrous Metals Society of China
www.tnmsc.cn

Constitutive relationship and characterization of fracture behavior for WE43 alloy under various stress states

Peng-fei WU[1], Chong ZHANG[1], Yan-shan LOU[1], Qiang CHEN[2], Hai-qing NING[2]

1. School of Mechanical Engineering, Xi'an Jiaotong University, Xi'an 710049, China;
2. Southwest Technology and Engineering Research Institute, Chongqing 400039, China

Received 14 October 2021; accepted 28 March 2022

Abstract: The plasticity and fracture behavior of the WE43 alloy were investigated under various stress states. Mechanical experiments were conducted with special designed specimens for tension, compression and shear. The testing process was recorded and handled by digital image correlation technology. Experimental results show that WE43 alloy possesses the low tension−compression asymmetry and the fracture mechanism belongs to the ductile fracture. The plastic deformation behavior under uniaxial tension and compression was simulated with different hardening laws based on the Drucker yield function. The stress state and fracture strain were obtained by the numerical simulation. The ductile fracture behavior was numerically predicted by Brozzo, Oh, Ko-Huh and DF2016 criteria to compare with the experimental results. The results suggest that the plastic deformation can be reasonably modeled by the Swift−Voce hardening law and Drucker yield function. It is also demonstrated that the DF2016 criterion can accurately predict the fracture behavior of the alloy under various stress states.

Key words: rare-earth magnesium alloy; plastic deformation behavior; stress state effect; constitutive model; ductile fracture prediction

1 Introduction

Magnesium (Mg) alloys possess outstanding properties and are applied in the fields of aerospace, military and transportation [1,2]. However, as a typical hexagonal close-packed (HCP) metal, Mg alloys show obvious difference between tension and compression, namely strength differential (SD) effect. Besides, the formability of Mg alloys is poor because of lacking enough active slip system at room temperature [3]. The accurate numerical simulation of plastic deformation and fracture is a big challenge for Mg alloys under different loading conditions.

A large number of isotropic yield functions were proposed to take account of the effect of three stress invariants on yield behavior of materials. The von Mises function is the most popular, which assumes that the plastic deformation occurs when the root-mean-square shear stress reaches a critical value. Another common yield function is the Drucker yield criterion [4]. CAZACU et al developed the Cazacu−Barlat2004 [5] and CPB2006 [6] yield functions to characterize the SD effect. YOON et al [7] and LOU et al [8] described the effect of the first stress invariant on the yield behavior of pressure-sensitive metals. HU and YOON [9] proposed an analytical description of Yoon2014 yield function to accurately describe the evolution of SD effect.

Generally, the failure of lightweight-high strength metal in the forming process is mainly caused by the ductile fracture (DF) [10]. Some ductile fracture

Corresponding author: Yan-shan LOU, Tel: +86-29-82664723, E-mail: ys.lou@xjtu.edu.cn;
Qiang CHEN, Tel: +86-23-68792286, E-mail: 2009chenqiang@163.com
DOI: 10.1016/S1003-6326(22)66118-1

criteria were proposed to model the fracture behavior under various stress states. One type is the coupled fracture criteria which consider the effect of damage on the deformation behavior of metals, for example, Gurson−Tvergaard−Needleman (GTN) and Continuum Damage Mechanics (CDM) models. YUE et al [11] simulated the fracture occurrence of a low carbon steel based on a fully coupled ductile damage model. ZHANG et al [12] used the advanced full CDM model to improve the failure prediction accuracy for AZ31B sheet forming simulation. Another type is the uncoupled fracture criteria which neglect the effect of damage on the plasticity, such as the traditional Cockcroft−Latham, Brozzo, Oh and Johnson−Cook models. MOHR and MARCACET [13] established the Mohr−Hosford fracture criterion to describe the fracture behavior of steels with high prediction accuracy. Based on the micro-mechanisms of damage accumulation, LOU et al [10,14,15] proposed the DF series criteria. Besides, LIAN et al [16,17] combined the features of coupled and uncoupled models to characterize the cold formability of steel.

Concerning the modeling for WE43 alloy, ZECEVIC et al [18] applied the viscoplastic self-consistent (VPSC) model to predict the mechanical response of WE43 alloy. FEATHER et al [19] investigated the anisotropic mechanical property of WE43 alloy through a multi-level crystal plasticity modeling, which shows good agreement with experiments. But, it is not easy to calibrate the material constants of those equations. The calculation time is relatively long due to the multi-iterative loops. These shortcomings make it very difficult to apply these models to the numerical simulation of the plastic deformation processes. Besides, there are rare reports on the fracture characterization of WE43 alloy, especially for the stress state effect.

In this research, the effect of stress state on the plasticity and fracture behavior of WE43 alloy is investigated, including tension, compression and shear. The plasticity is modeled by the Drucker yield function and the Swift−Voce hardening equation, and ductile fracture is described by various fracture criteria. The numerical prediction is compared with the experimental results to evaluate the performance of the constitutive models.

2 Experimental

2.1 Experimental procedure

The parent material of WE43 alloy with the size of 190 mm × 105 mm × 10 mm is fabricated by the rolling process and subsequent T6 thermal treatment. The chemical composition is listed in Table 1.

Table 1 Chemical composition of WE43 alloy (wt.%)

Y	Nd	Ce	La	Zr
3.7−4.3	2.4−3.0	0.3	0.2	0.5
Si	Fe	Cu	Ni	Mg
0.001	0.015	0.001	0.001	Bal.

The stress states include uniaxial tension, plane strain tension, uniaxial compression, plane strain compression and shear. These specimens are manufactured along the rolling direction. The two-dimensional drawings of all specimens are shown in Fig. 1, including smooth round bar (SRB), notched round bar (NRB), plane strain tension (PST), compression cylinder (CC), plane strain compression (PSC), notched compression cylinder (NCC) and in-plane torsion for shear (IPS) specimens. The testing experiments are performed on the 100 kN INSTRON universal testing machine except for IPS in Fig. 1(g), which is tested by the in-house developed in-plane torsion device [20]. These specimens are painted with white on the surface and dried for about 3 min, followed by sprinkling of black paint to develop a random speckled pattern. The deformation processes are recorded by the XTOP-3D digital image correlation (DIC) system. The system synthesizes the reaction force input from the load cell of the universal testing machine at the identical rate with the recorded images. The collection frequency is adjusted so that about 200 images with the resolution of 2448 × 2048 are recorded. Because the signal from the load cell is synthesized by the 3D-DIC system, the load−stroke curves are obtained directly. The torsion angle is measured by the 3D-DIC system and then the torque−torsion angle relation is obtained by interpolation between torsion angle−time curves and torque−time curves. To ensure the reliability and repeatability of experimental data, each experiment is carried out at least four times.

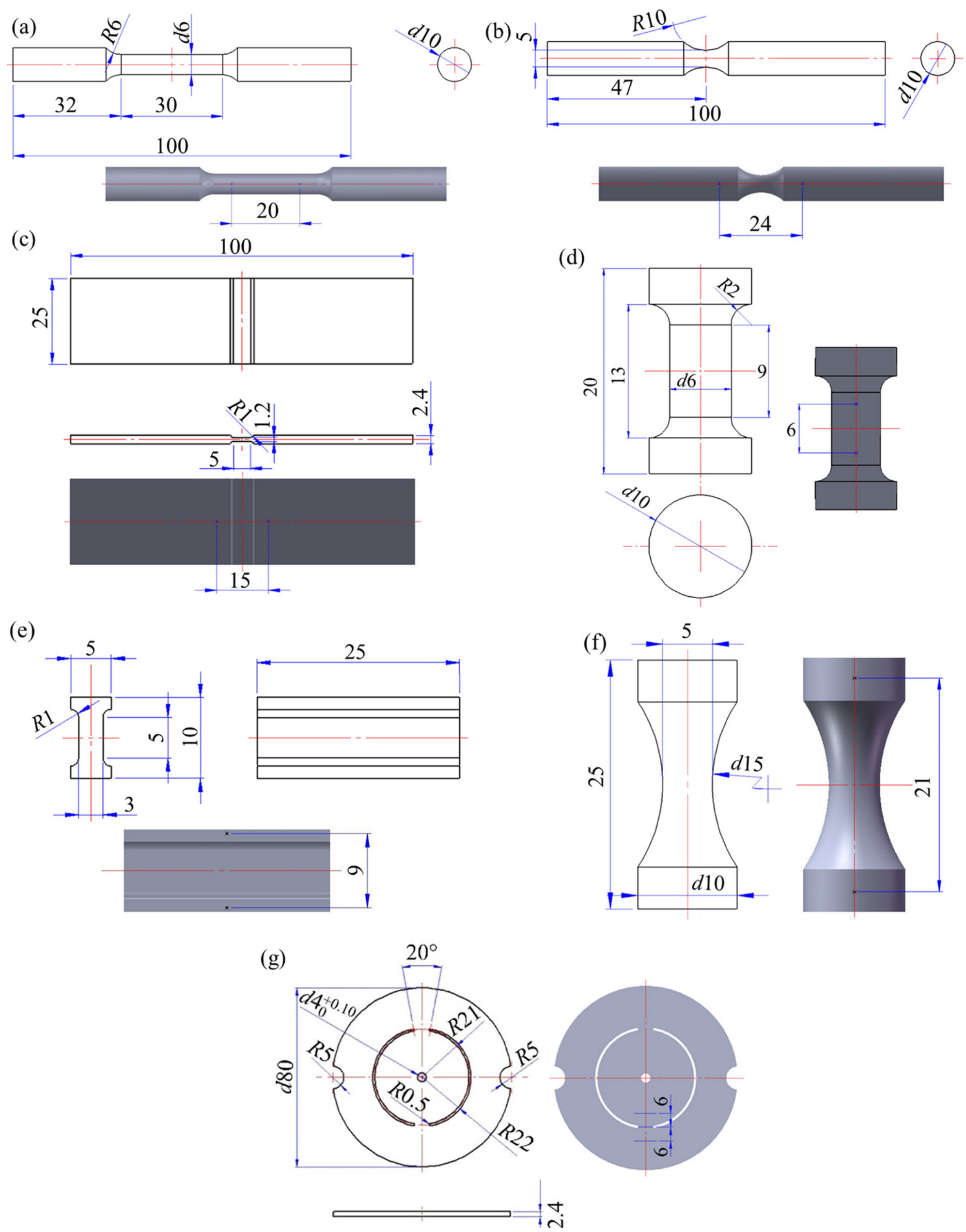

Fig. 1 Testing specimens under different stress states: (a) SRB; (b) NRB; (c) PST; (d) CC; (e) PSC; (f) NCC; (g) IPS (unit: mm)

2.2 Experimental result

The load−stroke curves for SRB and CC specimens are presented in Fig. 2. Three results are compared, which show high repeatability of the experiments. These specimens quickly yield as the force increases, and enter the stage of the elastic-plastic deformation. After reaching the maximum force, the SRB specimens fracture almost instantly with no apparent necking. This can be confirmed by the macroscopic fracture surface of the SRB specimen in Fig. 3(a). The fracture surface of SRB specimen inclined to the tensile stress is called the oblique fracture. This is the typical fracture of cup-cone shape with the gray and dark sections. The macro fracture of SRB specimen is composed of three parts: the fiber zone, radiation zone and shear lip zone, as presented in Fig. 3(a). The fracture of CC specimens occurs suddenly when the reaction force still rises. The fracture surface presented in Fig. 3(b) is the typical shear fracture which is about 45° to the compression axis. It is clearly seen that there are obvious macroscopic plastic deformation marks from the fracture surface. The fracture mechanism of WE43 alloy belongs to

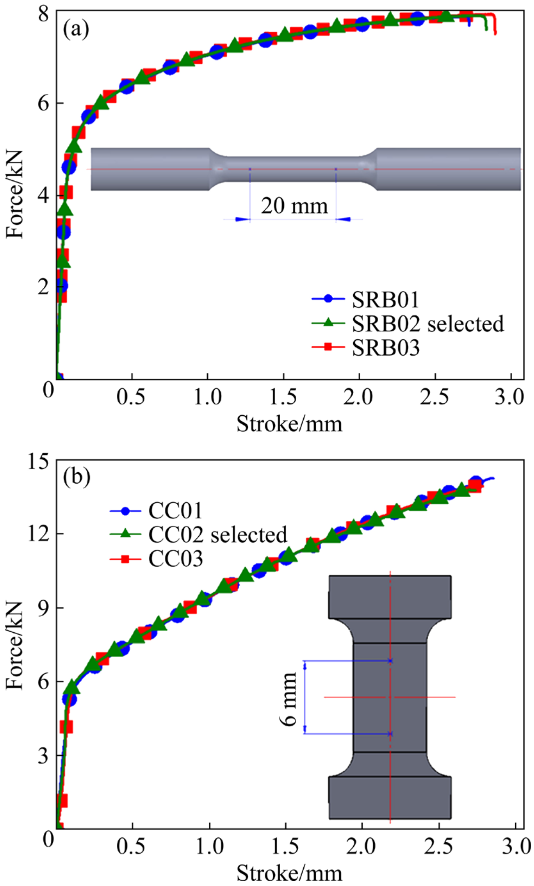

Fig. 2 Force−stroke curves for SRB (a) and CC (b) specimens

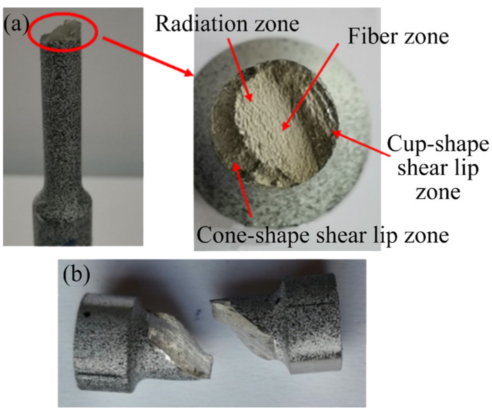

Fig. 3 Fracture surfaces of SRB (a) and CC (b) specimens

ductile fracture and fracture obviously occurs before necking. The maximum force can be regarded as the fracture onset for SRB and CC specimens.

The true stress−true plastic strain relationships under uniaxial tension and compression stress states are shown in Fig. 4. It is seen that the yield stress is very similar under uniaxial tension and compression, which is approximately 150 MPa. The strength difference between tension and compression is much low, which is different from the common Mg alloys, such as AZ31 [21]. This is due to the effect of rare earth elements.

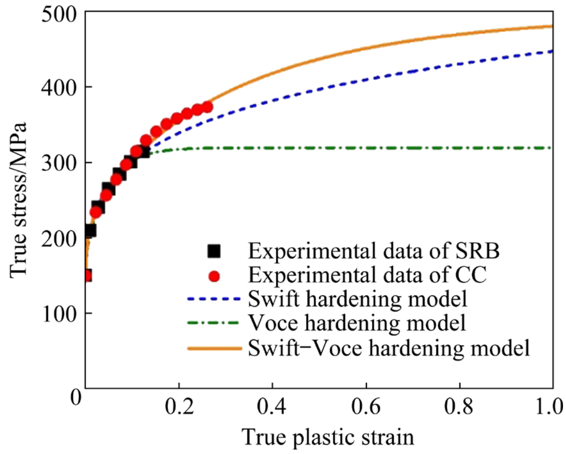

Fig. 4 Comparison of experimental true stress−true plastic strain curves and calibrated results under various hardening models

3 Material model

3.1 Hardening model

The metals generally present the classical work-hardening behavior during the plastic deformation process. The plastic flow can be expressed by various hardening models, such as Swift, Voce and Swift−Voce equations respectively as follows:

$$\bar{\sigma}=k(\varepsilon_0+\varepsilon_{\text{peeq}})^n \tag{1}$$

$$\bar{\sigma}=A-(A-B)\exp(-C\varepsilon_{\text{peeq}}) \tag{2}$$

$$\bar{\sigma}=\alpha k(\varepsilon_0+\varepsilon_{\text{peeq}})^n+(1-\alpha)[A-(A-B)\exp(-C\varepsilon_{\text{peeq}})] \tag{3}$$

where $\bar{\sigma}$ is the equivalent stress; $\varepsilon_{\text{peeq}}$ is the equivalent plastic strain (PEEQ), k, ε_0, n, A, B, and C are material constants calibrated by the corresponding mechanical experiment, and α is the proportional constant which is set to be 0.5 taking account of the comprehensive effect of Swift and Voce hardening model.

3.2 Isotropic yield function

The stress state of an isotropic material under three-dimensional loading can be solely determined by three stress invariants: the first stress invariant I_1, and the second and third deviator stress invariants denoted by J_2 and J_3. The three stress invariants are computed as follows:

$$I_1=\sigma_1+\sigma_2+\sigma_3=3\sigma_m \tag{4}$$

$$J_2=\frac{1}{2}s_{ij}s_{ij}=\frac{1}{6}[(s_1-s_2)^2+(s_2-s_3)^2+(s_3-s_1)^2] \tag{5}$$

$$J_3=\det(s_{ij})=s_1s_2s_3 \tag{6}$$

where σ_1, σ_2 and σ_3 represent three principal values of the stress tensor $\boldsymbol{\sigma}$, s_1, s_2 and s_3 denote three principal values of the stress deviator tensor $\boldsymbol{s}$, and σ_m is the mean stress which is a key parameter for pressure-sensitive material.

DRUCKER [4] proposed a yield criterion involving J_2 and J_3 with the form of

$$\bar{\sigma}=a(J_2^3-cJ_3^2)^{1/6}=\sigma_D \tag{7}$$

where a and c are two material constants, and σ_D is the Drucker yield stress. The yield function is also transformed into the Lode dependent form as follows [22]:

$$\bar{\sigma}=a\left\{\frac{1}{27}-c\frac{4L^2(L^2-9)^2}{729(L^2+3)^2}\right\}^{1/6}\sigma_{\text{Mises}}=\sigma_D \tag{8}$$

with

$$a=\left(\frac{1}{27}-c\frac{4}{729}\right)^{-1/6} \tag{9}$$

$$L=\frac{2\sigma_2-\sigma_1-\sigma_3}{\sigma_1-\sigma_3}=\frac{(\sigma_2-\sigma_3)-(\sigma_1-\sigma_2)}{\sigma_1-\sigma_3} \tag{10}$$

where L is Lode parameter. When the value of c is equal to zero, Eq. (7) reduces to the von Mises yield criterion.

Based on the deformation characteristics of WE43 alloy illustrated in Fig. 4, the Drucker yield function is selected to describe the yield behavior. Since WE43 belongs to an HCP metal, there is no suggestion for the value of c. In this study numerical simulation is carried out by using different values of parameter c, and it is found that the plasticity is reasonably described when c=2. Here, the value of parameter a is equal to 1.8652 according to LOU and YOON [22] when c=2. The yield loci under different plastic strains for the Drucker yield function are presented in Fig. 5.

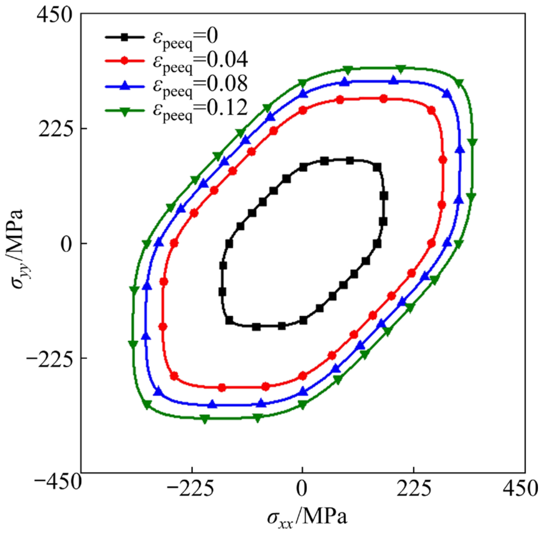

Fig. 5 Drucker yield loci under different plastic strains

3.3 Fracture criterion

Due to the poor computational efficiency and complicated calibration procedure, the application of coupled ductile fracture criteria is still limited. At the aspect of uncoupled ductile fracture criteria, COCKCROFT and LATHAM [23] considered that the initiation of fracture behavior is related to the maximum principal stress σ_1, and proposed a prediction model (C−L) with the following form:

$$\int_0^{\varepsilon_f}\sigma_1 d\varepsilon^p=C \tag{11}$$

where ε_f denotes the PEEQ at fracture onsets, $d\varepsilon^p$ is the equivalent plastic strain increment, and C is the material constant.

BROZZO et al [24] coupled the effect of hydrostatic pressure and maximum principal stress on ductile fracture, and proposed a ductile fracture model expressed as follows:

$$\int_0^{\varepsilon_f}\frac{2}{3}\left(1-\frac{\sigma_h}{\sigma_1}\right)^{-1}d\varepsilon^p=C \tag{12}$$

where σ_h represents the hydrostatic pressure.

Based on the C−L criterion, OH et al [25] replaced σ_I with the normalized maximum principal stress, namely,

$$\int_0^{\varepsilon_f}\frac{\sigma_1}{\bar{\sigma}}d\varepsilon^p=C \tag{13}$$

KO et al [26] modified the C−L criterion by combining the stress triaxiality and developed a ductile fracture criterion written as

$$\int_0^{\varepsilon_f}\frac{\sigma_1}{\bar{\sigma}}(1+3\eta)d\varepsilon^p=C \tag{14}$$

with

$$\eta = \frac{\sigma_{\mathrm{m}}}{\sigma_{\mathrm{Mises}}} = \frac{I_1}{3\sqrt{3J_2}} \tag{15}$$

where η is the stress triaxiality.

In recent years, a micro-mechanism-motivated phenomenological ductile fracture criterion has been proposed. From the observation of micro-mechanism, the ductile fracture includes void nucleation, growth and coalescence. Due to its high accuracy for multiple loading conditions, DF2016 fracture criterion [15] is widely applied to predicting the fracture strain of metal, which is expressed as

$$\left(\frac{2\tau_{\max}}{\sigma_{\mathrm{Mises}}}\right)^{C_1}\left(\frac{f(\eta,L,C)}{f(1/3,-1,C)}\right)^{C_2}\varepsilon_{\mathrm{f}} = C_3 \tag{16}$$

The function $f(\eta, L, C)$ is suggested to write in the form of

$$f(\eta,L,C) = \eta + C_4\frac{(3-L)}{3\sqrt{L^2+3}} + C \tag{17}$$

where $\tau_{\max}$ is the maximum shear stress, C_1, C_2, C_3 and C_4 are four fracture parameters, and C is introduced to consider the effect of L on the void shape change during the deformation process.

The effect of $\tau_{\max}$ on ductile fracture can be equivalent to that of L on shear voids coalescence. Equation (16) can be also expressed as

$$\left(\frac{2}{\sqrt{L^2+3}}\right)^{C_1}\left(\frac{f(\eta,L,C)}{f(1/3,-1,C)}\right)^{C_2}\varepsilon_{\mathrm{f}} = C_3 \tag{18}$$

Generally, the ductile fracture is viewed as a cumulative process in numerical prediction. Therefore, Eq. (16) can be expressed by an integral form as follows:

$$D = \int_0^{\varepsilon_{\mathrm{f}}}\frac{1}{C_3}\left(\frac{2}{\sqrt{L^2+3}}\right)^{C_1}\left(\frac{f(\eta,L,C)}{f(1/3,-1,C)}\right)^{C_2}\mathrm{d}\varepsilon^{\mathrm{p}} \tag{19}$$

where D is the value of cumulative damage, which changes from 0 to 1. Failure occurs for materials when D=1.

4 FE simulation for hardening behavior

4.1 FE model

The FE models with 1/4 (Figs. 1(a−f)) or 1/2 (Fig. 1(g)) structure are established based on the Hypermesh and ABAQUS software, as shown in Fig. 6. Some key parameters are summarized in Table 2. The settings of FE models are as follows.

(1) The element adopts the eight-node linear brick with reduced integration (C3D8R), and the minimum size of mesh is 0.2 mm.

(2) The *XZ* and *XY* planes for SRB, NRB, PST, CC, PSC and NCC specimens are set to be planar symmetry, the bottom end is fixed, and the loading velocity is implemented on the top end.

(3) For the IPS specimen, the FE model is plane-symmetric with respect to the *XY* plane and the inner circle is fixed.

(4) Based on the loading condition of quasi-static strain rate, the imposed velocity is set to be 1.8, 0.8, 0.4, 0.6, 0.5 and 0.8 mm/min for SRB, NRB, PST, CC, PSC and NCC specimens, respectively.

(5) The rotating speed of IPS specimen is set to be 0.045 (°)/s, which is coincident with in-plane torsion device.

(6) The analysis step of FE model adopts the ABAQUS/Explicit mode.

4.2 Calibration of hardening model

By adopting the unconstrained nonlinear optimization method, the material constants of Swift, Voce and Swift−Voce hardening equations are calibrated based on the experimental data of SRB and CC specimens presented in Fig. 4. These material constants are summarized in Table 3. The comparison between the experimental true stress−true plastic strain curve and predicted results of various hardening models is shown in Fig. 4. It is seen that the predicted curves of three hardening models have a high agreement with the experimental result for the uniaxial tension loading. The Swift−Voce hardening model has a higher prediction accuracy than the Swift and Voce equations for the uniaxial compression loading. To compare the prediction accuracy of different hardening models more intuitively, the comparison of numerical and experiment results for SRB and CC specimens is shown in the following section.

4.3 FE simulation result

A VUMAT material subroutine of ABAQUS/ Explicit is developed for these hardening models, the Drucker yield function and various fracture criteria. The Drucker yield function is implemented

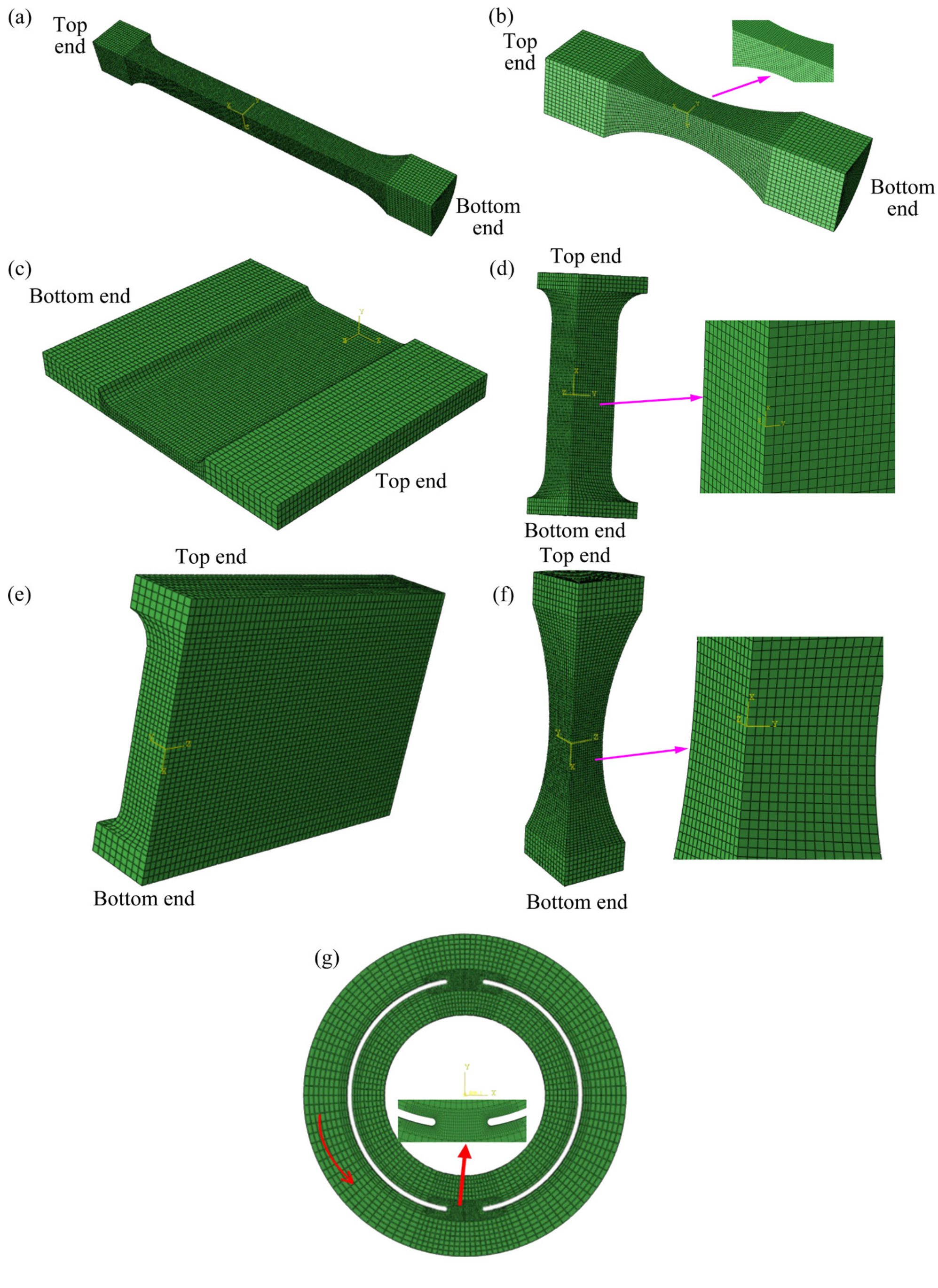

Fig. 6 FE models for different specimens: (a) SRB; (b) NRB; (c) PST; (d) CC; (e) PSC; (f) NCC; (g) IPS

Table 2 Key parameters of FE model

Parameter	Value or type
Velocity/ $(\mathrm{mm \cdot min^{-1}})$	1.8 (SRB), 0.8 (NRB), 0.4 (PST), 0.6 (CC), 0.5 (PSC), 0.8 (NCC), and 0.045 (°)/s (IPS)
Elastic modulus/GPa	45
Poisson ratio	0.35
Element type	C3D8R
Total time/s	100, 90, 110, 315, 135, 260 and 55

Table 3 Calibrated material constants of three hardening models for WE43 alloy

Material constant	Swift model	Voce model	Swift−Voce model
k/GPa	0.44787		0.30874
ε_0	0.0026		9.98×10^{-5}
n	0.17336		0.42019
A/GPa		0.31987	0.60419
B/GPa		0.17573	0.35484
C		21.23626	8.84985
α			0.5

into ABAQUS/Explicit using the backward Euler method. When the subroutine is called for the elastic-plastic FE analysis, an update algorithm based on the stress compensation is adopted according to the ABAQUS User Subroutines Reference Guide (6.14). The flow chart of the FE simulation with VUMAT is shown in Fig. 7. Firstly, it is assumed that the all strain increments are elastic. The trial stress σ_s^{tr} is calculated according to the generalized Hooke's law. Then, the values of σ_s^{tr} and yield stress σ_{yield} are calculated based on the material model and compared to check whether the plastic deformation occurs. If the value of σ_s^{tr} is less than the value of σ_{yield}, the material deformation is elastic and the stress update is directly completed. Otherwise, the plastic strain increment is calculated. The stress compensation update algorithm is used to update the stress components and PEEQ. Finally, the damage accumulation D is calculated by the damage fracture criterion. When the value of D is less than 1, the numerical iteration continues. Otherwise, the fracture behavior initiates with element deletion.

FE simulation of each specimen is ended when the numerical loading stroke reaches the average stroke of three repeating experiments. Because there is no plastic deformation in the cylindrical

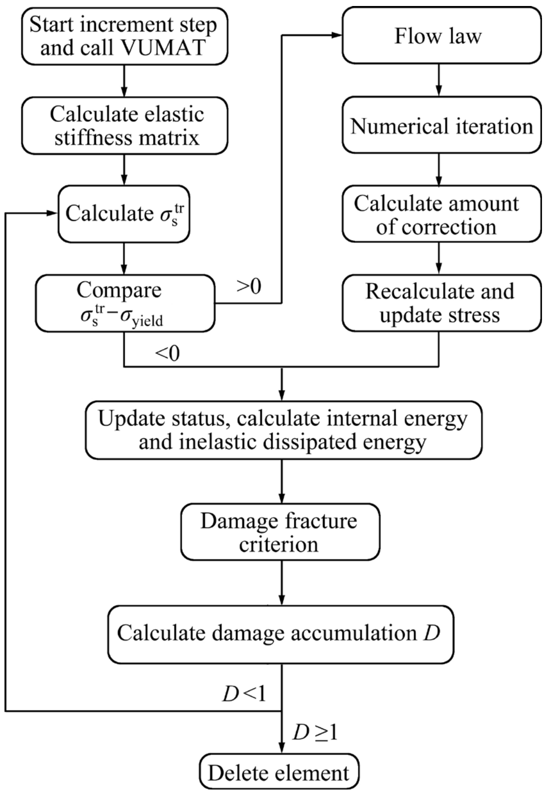

Fig. 7 Flow chart of FE simulation with VUMAT

section with d10 mm for CC specimen, the 16 mm height along the axis shown in Fig. 8(b) is selected as the initial gauge of the force−stoke curve. The numerical force−stroke curves for the three hardening models are compared with the experimental results for SRB and CC specimens, as shown in Figs. 8(a) and (b), respectively. It is seen that the modeled force−stroke curves under uniaxial tension have a small prediction error while the prediction accuracy of the Swift−Voce equation for uniaxial compression is higher than that of the Swift and Voce equations. The predicted phenomenon is very similar to that of true stress−true plastic strain curves. The result clearly shows that the numerical prediction of the Swift−Voce model has a higher consistency with the experimental result. Therefore, the Swift−Voce equation is selected as the hardening model of WE43 alloy. Besides, the result also implies that the material constants of the Drucker yield function and Swift−Voce equation are reliable.

5 Simulation of fracture behavior

5.1 Determination of fracture-related (F-R) variables

The material constants of DF2016 fracture criterion are calibrated by the experimental results of NRB, PST, PSC, NCC and IPS specimens. Generally, the F-R variables include the fracture strain ε_f, stress triaxiality η and Lode parameter L. Because the values of η and L at the fracture position are changeable, which are related to the deformation history, it is difficult to obtain the designed value by the experiment. Therefore, a hybrid experimental−numerical method is adopted to obtain the F-R variables.

An assumption is implicitly followed that if the predicted result of FE simulation is coincident with the experimental force−stroke curve, the FE predictions of stress and strain tensors in whole field of specimen are in agreement with the corresponding actual ones [23]. Based on the FE models presented in Fig. 6 and material models of the Drucker yield function and Swift−Voce hardening equation, the numerical simulations of NRB, PST, PSC, NCC and IPS specimens are carried out. The force−stroke curves are compared between the experiment and simulation, which are illustrated in Figs. 8(c−g). The predicted force−

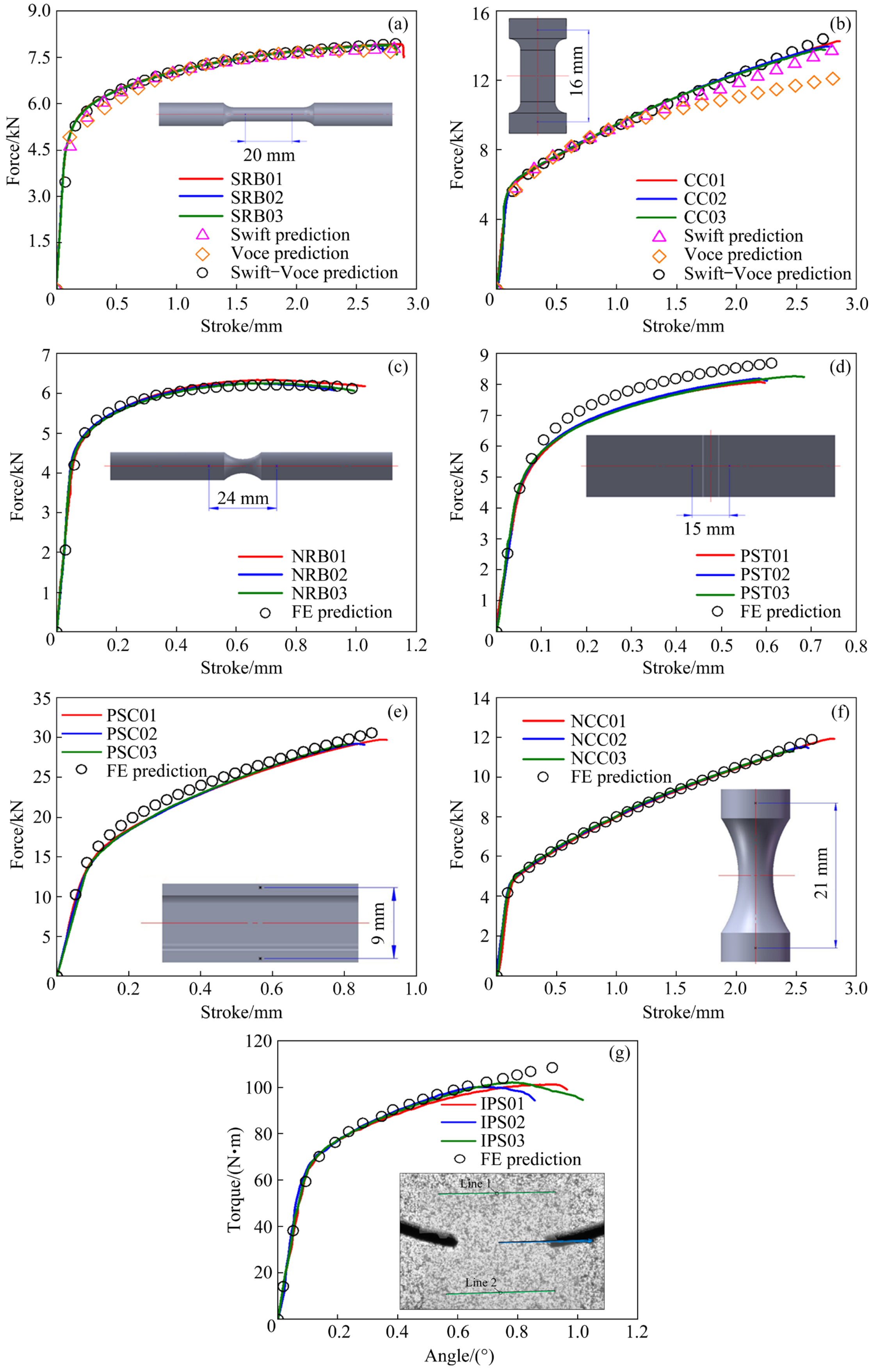

Fig. 8 Comparison between numerical and experimental results for force−stroke curves of different specimens: (a) SRB; (b) CC; (c) NRB; (d) PST; (e) PSC; (f) NCC; (g) IPS

stroke curves are close to the experimental results, and the accuracy is acceptable. The result indicates that the established material model can simulate the deformation behavior of WE43 alloy under various stress states with high accuracy. Besides, it is observed that the experimental torque of the in-plane shear test declines. This is expected to be due to the damage or micro-cracks around the notch edges where the strain is much larger than that in other areas.

Here, other assumption is set that the fracture behavior occurs at the position with the highest PEEQ, and the highest PEEQ can be regarded as the fracture strain [27]. The equivalent von Mises strains of NRB, PST, PSC, NCC and IPS specimens are extracted from the numerical results, as shown in Fig. 9. It is observed that the fracture strain locates at the center of the gauge for NRB and NCC specimens, at the middle of the gauge for PST specimen, and on the surface of the gauge for PSC and IPS specimens. Figure 9 also presents the comparison of the numerical and experimental results for the strain distribution, where the experimental data are taken from the last picture before fracture captured by 3D-DIC system. The deformation contour of the FE simulation is in high accordance with the result measured by DIC technology. The result indicates that the numerical simulation is accurate enough to represent the plastic deformation up to the ultimate fracture.

The highest PEEQ at fracture instants for NRB, PST, PSC and NCC specimens is selected as the fracture strain. The middle position of shear band is closer to the shear stress state than other zone for IPS specimen. The PEEQ value of the element in the middle position of shear band is adopted as the fracture strain. The values of η and L usually constantly change during the plastic deformation for the element of fracture strain, as shown in Fig. 10. The average values of η and L are computed as follows [27]:

$$\bar{\eta}=\frac{1}{\varepsilon_{\mathrm{f}}}\int_{0}^{\varepsilon_{\mathrm{f}}}\eta\varepsilon_{\mathrm{peeq}}\mathrm{d}\varepsilon_{\mathrm{peeq}} \tag{20}$$

$$\bar{L}=\frac{1}{\varepsilon_{\mathrm{f}}}\int_{0}^{\varepsilon_{\mathrm{f}}}L\varepsilon_{\mathrm{peeq}}\mathrm{d}\varepsilon_{\mathrm{peeq}} \tag{21}$$

The F-R variables are determined and listed in Table 4. The stress states of these specimens in the space of (η, L) are presented in Fig. 11. It is seen that the stress states of NRB, NCC and IPS specimens are close to the ideal stress state. But PST and PSC specimens are relatively away from the plane strain tension and compression stress states.

5.2 Calibration of fracture criteria

Based on the data listed in Table 4, the material constants of Brozzo, Oh, Ko and DF2016 fracture criteria are calibrated by using the optimization method. The error (E_{r}) between the calculated value and experimental data is computed as follows:

$$E_{\mathrm{r}}=\sum_{1}^{m}\left(\frac{\varepsilon_{j\text{-pre}}^{\mathrm{f}}-\varepsilon_{j\text{-exp}}^{\mathrm{f}}}{\varepsilon_{j\text{-exp}}^{\mathrm{f}}}\right)^{2} \tag{22}$$

where m is the number of input data, and $\varepsilon_{j\text{-pre}}^{\mathrm{f}}$ and $\varepsilon_{j\text{-exp}}^{\mathrm{f}}$ represent the predicted value and experimental result, respectively. The value of material constant C in Brozzo, Oh and Ko fracture criteria is calibrated as 0.3777, 0.3405 and 0.9496, respectively. The material constants of DF2016 fracture criterion are summarized in Table 5.

5.3 Comparison between predicted and experimental results

The predicted surfaces of fracture strain in the space of (η, L, ε_{f}) are presented in Fig. 12. It is clearly observed that these experimental fracture strains are distributed on both sides of the predicted surfaces for Brozzo, Oh and Ko fracture criteria. However, the five experimental fracture strains fall well on the predicted surface of DF2016 fracture criterion. The result indicates that the theoretical prediction accuracy of DF2016 fracture criterion is higher than that of the other three fracture criteria.

In order to further compare the prediction accuracy of different ductile fracture criteria, the FE simulations for NRB, PST, PSC, NCC and IPS specimens are conducted. The numerical force−stroke curves are compared with the experimental data, as presented in Fig. 13. The predicted fracture instants of Brozzo, Oh and Ko fracture criteria have a great difference with the experimental fracture situation. For DF2016 fracture criterion, the numerical force−stroke curves under different stress states are very close to the actual one with a small difference. The result indicates that DF2016 fracture criterion is more suitable for predicting the fracture behavior of WE43 alloy than Brozzo, Oh and Ko fracture criteria.

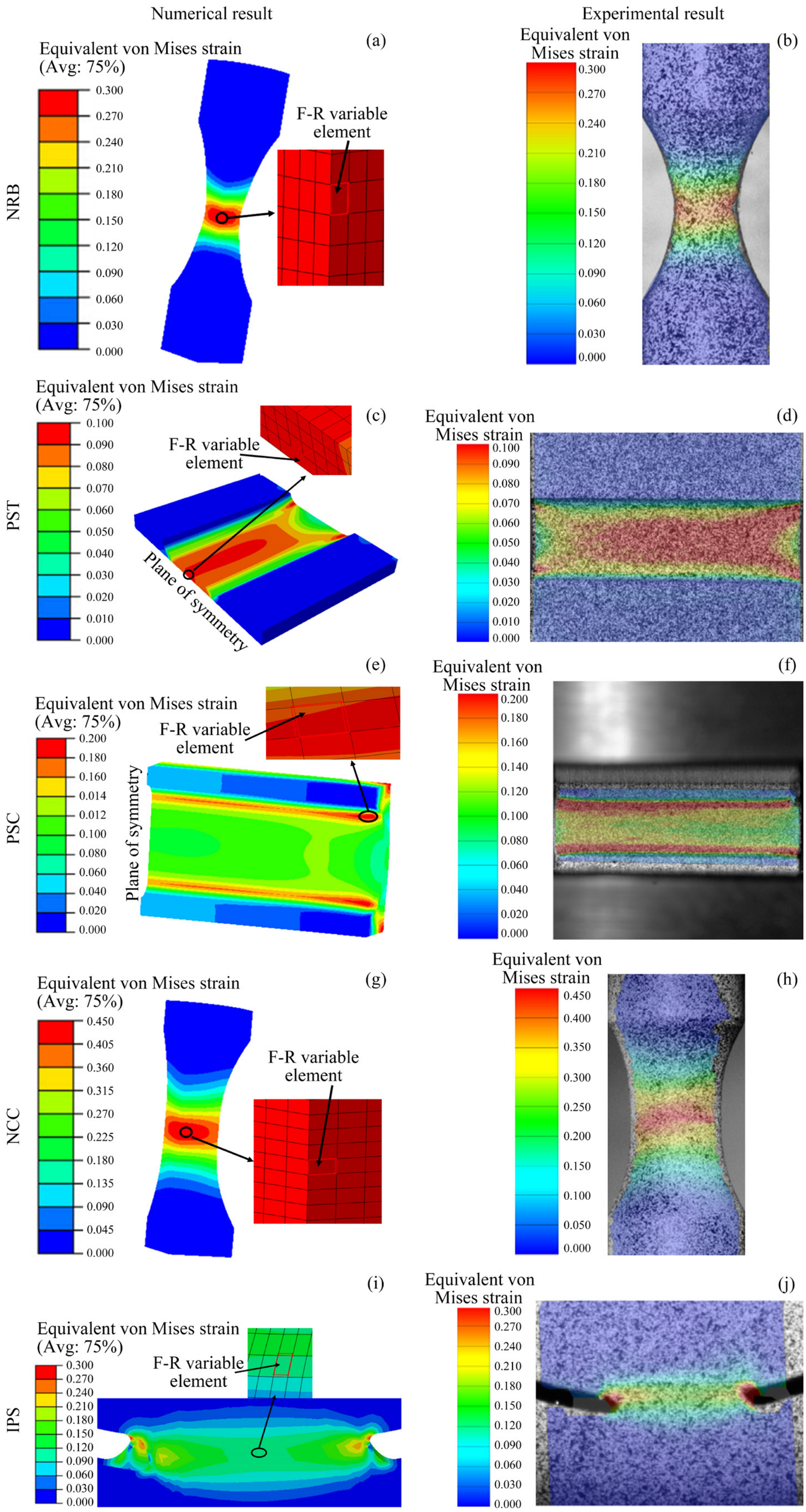

Fig. 9 Deformation contour and equivalent von Mises strain distribution at fracture instant in FE simulation (a, c, e, g, i) and experiment (b, d, f, h, j)

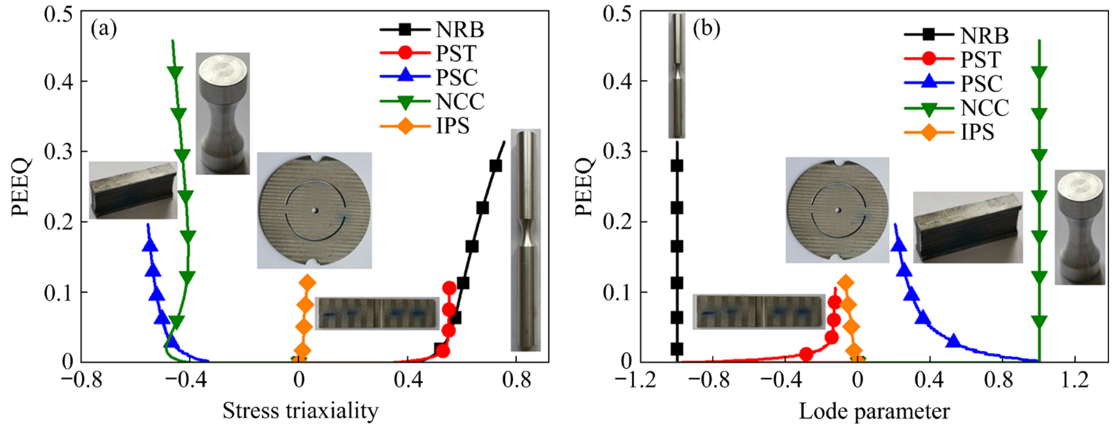

Fig. 10 Evolution of stress states for different specimens: (a) Stress triaxiality; (b) Lode parameter

Table 4 Fracture strain and stress state of testing specimens

Specimen	Fracture position	η	L	ε_f
NRB	Neck center	0.63031	−0.99933	0.31356
PST	Middle plane	0.53563	−0.19549	0.10791
PSC	Gauge surface	−0.50867	0.35866	0.19522
NCC	Neck center	−0.43396	0.99985	0.45801
IPS	Gauge surface	0.01922	−0.04118	0.11341

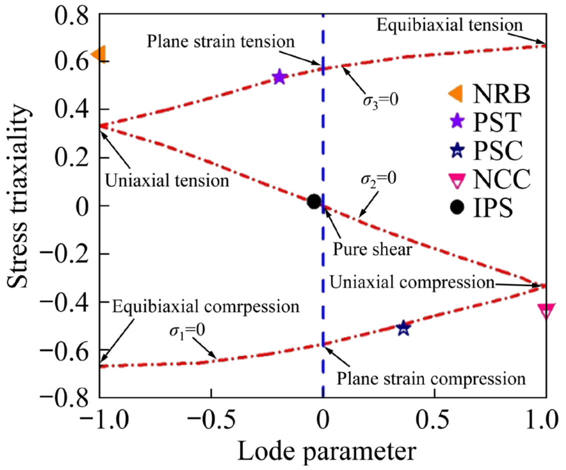

Fig. 11 Stress states of testing specimens

Table 5 Material constants of DF2016 ductile fracture criterion

C	C_1	C_2	C_3	C_4
2.2051	8.1718	0.8919	0.2878	−0.6153

Figure 14 shows the deformation region of WE43 alloy under different stress states. The inner black locus is the Drucker yield surface which indicates the onset of plastic deformation. The outer red locus is the calibrated DF2016 fracture locus which is transformed from the strain space to the stress space based on the calibrated Swift−Voce hardening law and the Drucker yield function. The evolving equivalent stress for SRB, CC, PST, PSC and IPS specimens is also plotted in Fig. 14. It is seen that the plastic deformation under different stress states is between the yield surface and fracture stress locus. The result proves the reliability of the established DF2016 fracture criterion.

The predicted fracture contours of DF2016 fracture criterion for NRB, PST, PSC, NCC and IPS specimens are presented in Fig. 15. Fracture moments of NRB, PST, PSC and IPS specimens in the experimental process are captured by 3D-DIC system. Different from other specimens, NCC specimen is out of the observable field of 3D-DIC system at the moment of fracture. It is clearly shown that the predicated fracture contours of DF2016 fracture criterion have a high agreement with the experimental fracture phenomenon. Besides, the ductile fracture of tension type mainly concentrates in the central position, that of compression type shows an oblique angle, and that of torsional in-plane shear is close to the edge of the inner ring.

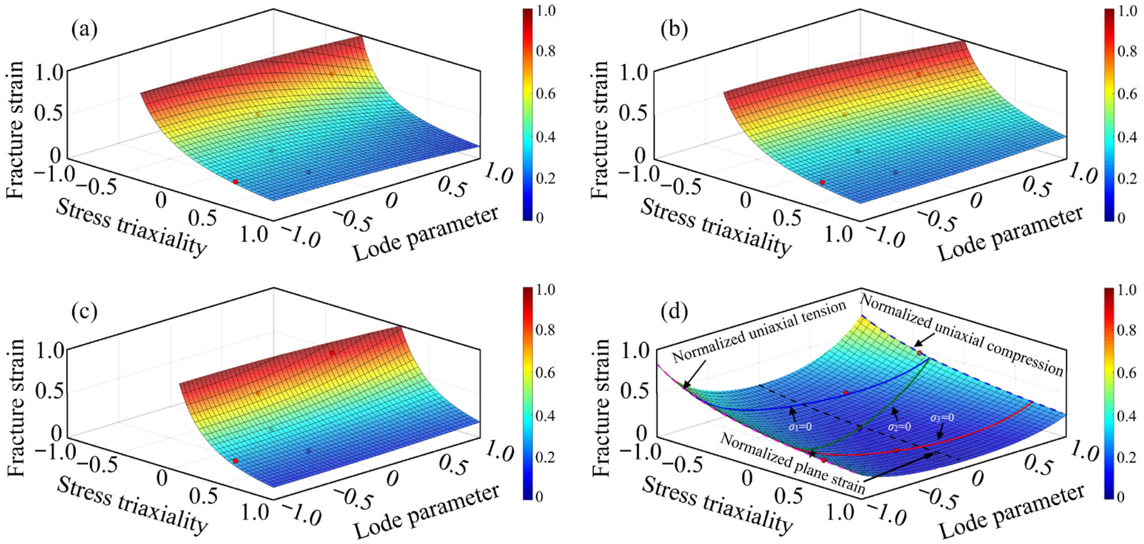

Fig. 12 Prediction of fracture strain for Brozzo (a), Oh (b), Ko (c) and DF2016 (d) fracture criteria

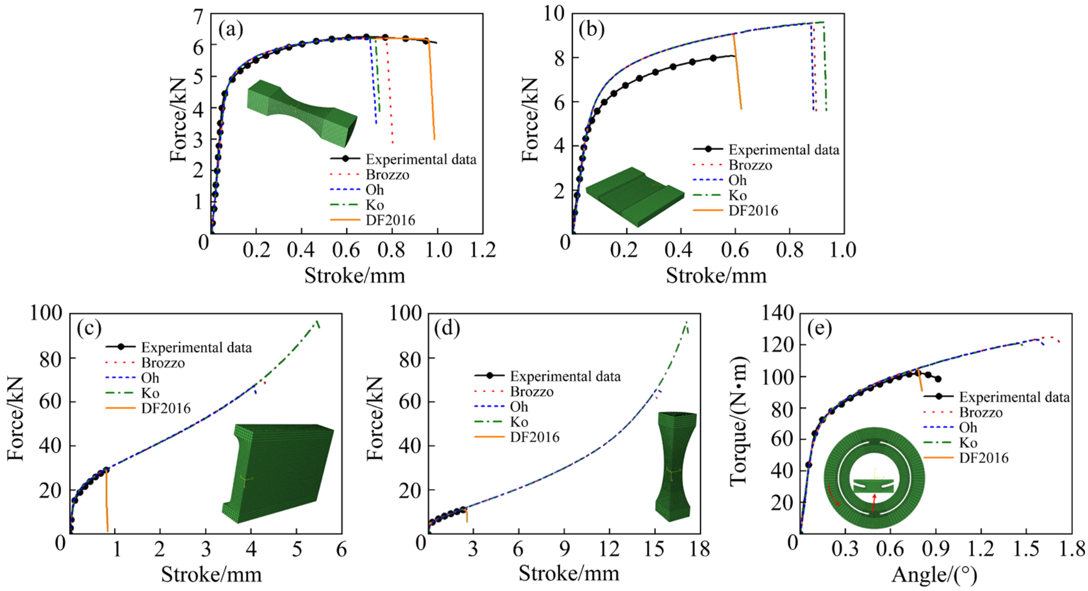

Fig. 13 Comparison of FE prediction and experimental results for different specimens: (a) NRB; (b) PST; (c) PSC; (d) NCC; (e) IPS

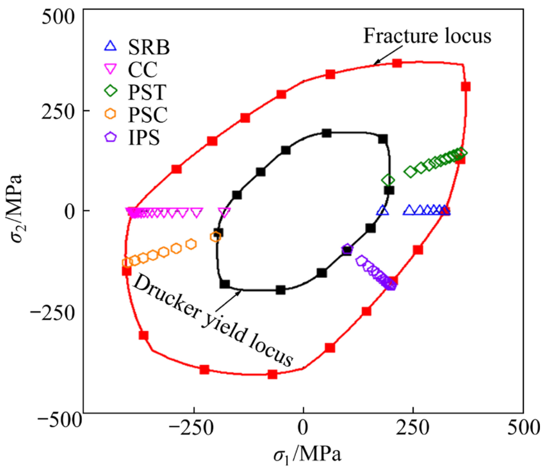

Fig. 14 Plastic flow region of WE43 alloy in plane principal stress space (σ_1, σ_2)

6 Prediction of plastic behavior for NRB specimen with external notch radius of 20 mm

The mechanical experiment and FE simulation of the NRB specimen with external notch radius of 20 mm (R=20 mm) are carried out to prove the applicability of the established model. The calculated fracture strain (black pentagram) of DF2016 fracture criterion is plotted in Fig. 12(d). Figure 16 presents the comparison between the numerical result and experimental data. It is seen that the predicted result has a high consistency with the experimental data. The fracture contours of FE and experiment are basically similar, as shown in Fig. 17. The fracture of the specimen occurs instantly at the neck center of the gauge, presenting a classical ductile fracture.

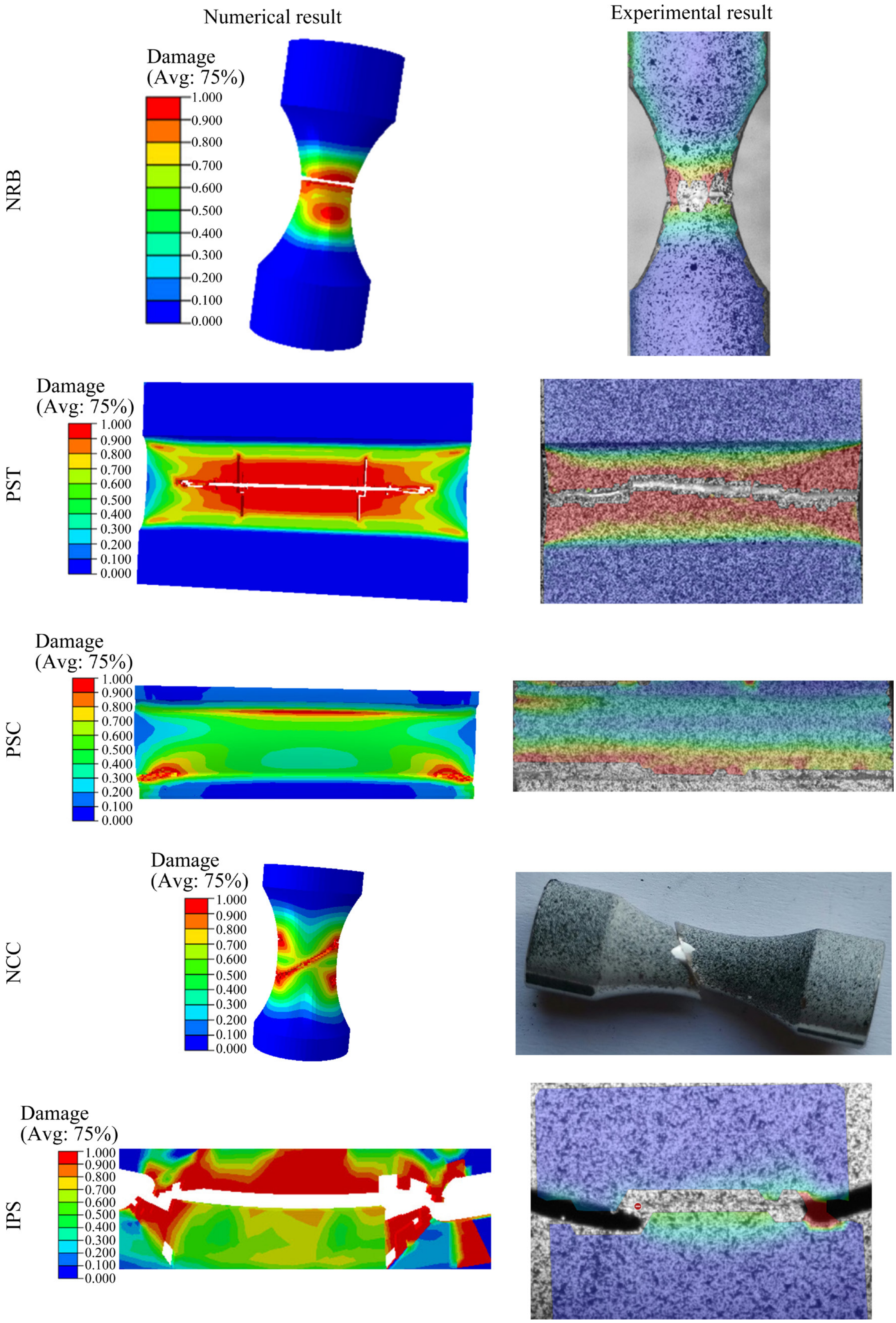

Fig. 15 Predicted fracture contours of DF2016 fracture criterion for different specimens

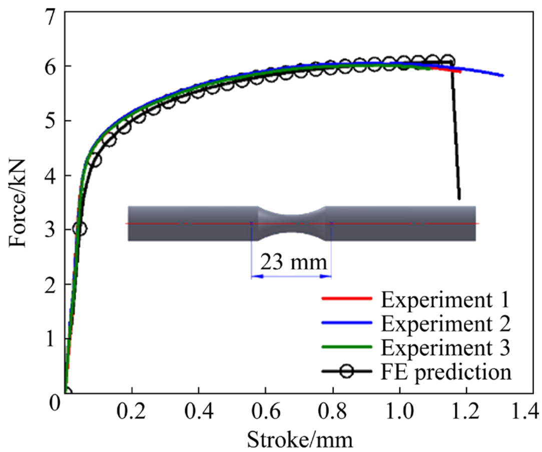

Fig. 16 Comparison of numerical force−stroke curve and experimental result for NRB specimen with R=20 mm

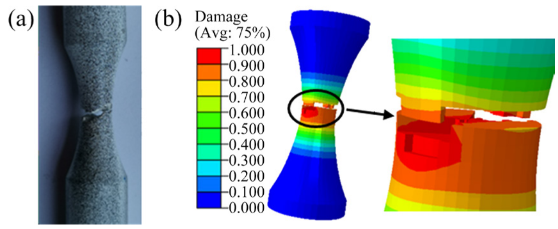

Fig. 17 Comparison of experimental (a) and numerical (b) fracture contours for NRB specimen with R=20 mm

7 Conclusions

(1) From the experiment result of SRB and CC specimens, it is ensured that the fracture mechanism of WE43 alloy belongs to ductile fracture.

(2) By comparing the true stress−true plastic strain curves under the uniaxial tension and compression stress states, it is found that the strength of tension and compression states is very similar, showing a lower tension−compression asymmetry.

(3) The Swift−Voce hardening equation can well characterize the hardening phenomenon of WE43 alloy under the uniaxial tension and compression stress states.

(4) The F-R variables under various stress states are obtained by a hybrid experimental−numerical method. Through the comparison for the fracture behavior prediction, DF2016 criterion is shown to be capable of providing reasonable prediction, and the fracture morphology is well modeled by the FE simulation.

(5) The numerical simulation and experiment of NRB specimen with R=20 mm are conducted to verify the prediction accuracy of the established model. It suggests that the calibrated model can be used to model plasticity and fracture onset for WE43 alloy.

Acknowledgments

The authors acknowledge the financial support from the National Natural Science Foundation of China (No. 52075423), the State Key Laboratory of Mechanical System and Vibration (No. MSV202009), and the State Key Laboratory of High Performance Complex Manufacturing, China (No. Kfkt2019-02).

References

[1] BAZHENOV V E, SAIDOV S S, TSELOVALNIK Y V, VOROPAEVA O O, PLISETSKAYA I V, TOKAR A A, BAZLOV A I, BAUTIN V A, KOMISSAROV A A, KOLTYGIN A V, BELOV V D. Comparison of castability, mechanical, and corrosion properties of Mg−Zn−Y−Zr alloys containing LPSO and W phases [J]. Transactions of Nonferrous Metals Society of China, 2021, 31(5): 1276−1290.

[2] LIANG Xin-li, PENG Xiang, JI Hao, LIU Wen-cai, WU Guo-hua, DING Wen-jiang. Microstructure and mechanical properties of as-cast and solid solution treated Mg−8Li−xAl−yZn alloys [J]. Transactions of Nonferrous Metals Society of China, 2021, 31(4): 925−938.

[3] CHAMAN-ARA M, EBRAHIMI G R, EZATPOUR H R. Deformation behavior and processing maps of Mg−Zn−Y alloy containing I phase at elevated temperatures [J]. Transactions of Nonferrous Metals Society of China, 2018, 28(4): 629−641.

[4] DRUCKER D C. Relation of experiments to mathematical theories of plasticity [J]. Journal of Applied Mechanics, 1949, 16(4): 349−357.

[5] CAZACU O, BARLAT F. A criterion for description of anisotropy and yield differential effects in pressure-insensitive metals [J]. International Journal of Plasticity, 2004, 20(11): 2027−2045.

[6] CAZACU O, PLUNKETT B, BARLAT F. Orthotropic yield criterion for hexagonal closed packed metals [J]. International Journal of Plasticity, 2006, 22(7): 1171−1194.

[7] YOON J W, LOU Y S, YOON J H, GLAZOFF M V. Asymmetric yield function based on the stress invariants for pressure sensitive metals [J]. International Journal of Plasticity, 2014, 56: 184−202.

[8] LOU Y S, ZHANG S J, YOON J W. Strength modeling of sheet metals from shear to plane strain tension [J]. International Journal of Plasticity, 2020, 134: 102813.

[9] HU Q, YOON J W. Analytical description of an asymmetric yield function (Yoon2014) by considering anisotropic hardening under non-associated flow rule [J]. International Journal of Plasticity, 2021, 140: 102978.

[10] LOU Y S, YOON J W, HUH H. Modeling of shear ductile fracture considering a changeable cut-off value for stress triaxiality [J]. International Journal of Plasticity, 2014, 54: 56−80.

[11] YUE Z, CAO K, BADREDDINE H, SAANOUNI K, GAO J. Failure prediction on steel sheet under different loading paths based on fully coupled ductile damage model [J]. International Journal of Mechanical Sciences, 2019, 153/154: 1−9.

[12] ZHANG K, BADREDDINE H, YUE Z M, HFAIEDH N, SAANOUNI K, LIU J L. Failure prediction of magnesium alloys based on improved CDM model [J]. International Journal of Solids and Structures, 2021, 217/218: 155−177.

[13] MOHR D, MARCADET S J. Micromechanically-motivated phenomenological Hosford Coulomb model for predicting ductile fracture initiation at low stress triaxialities [J]. International Journal of Solids and Structures, 2015, 67/68: 40−55.

[14] LOU Y S, HUH H, LIM S J, PACK K K H. New ductile fracture criterion for prediction of fracture forming limit diagrams of sheet metals [J]. International Journal of Solids and Structures, 2012, 49: 3605−3615.

[15] LOU Y S, CHEN L, CLAUSMEYER T, TEKKAYA A E, YOON J W. Modeling of ductile fracture from shear to balanced biaxial tension for sheet metals [J]. International Journal of Solids and Structures, 2017, 112: 169−184.

[16] LIAN J, SHARAF M, ARCHIE F, MÜNSTERMANN S. A hybrid approach for modelling of plasticity and failure behaviour of advanced high-strength steel sheets [J]. International Journal of Damage Mechanics, 2013, 22(2): 188−218.

[17] LIAN J, WU J, MÜNSTERMANN S. Evaluation of the cold formability of high-strength low-alloy steel plates with the modified Bai−Wierzbicki damage model [J]. International Journal of Damage Mechanics, 2015, 24(3): 383−417.

[18] ZECEVIC M, KNEZEVIC M, MCWILLIAMS B, LEBENSOHN R A. Modeling of the thermo-mechanical response and texture evolution of WE43 Mg alloy in the dynamic recrystallization regime using a viscoplastic self-consistent formulation [J]. International Journal of Plasticity, 2020, 130: 102705.

[19] FEATHER W G, GHORBANPOUR S, SAVAGE D J, ARDELJAN M, JAHEDI M, MCWILLIAMS B A, GUPTA N, XIANG C C, VOGEL S C, KNEZEVIC M. Mechanical response, twinning, and texture evolution of WE43 magnesium−rare earth alloy as a function of strain rate: Experiments and multi-level crystal plasticity modeling [J]. International Journal of Plasticity, 2019, 120: 180−204.

[20] ZHANG C, LOU Y S, ZHANG S J, CLAUSMEYER T, TEKKAYA A E, FU L, CHEN Q, ZHANG Q. Large strain flow curve identification for sheet metals under complex stress states [J]. Mechanics of Materials, 2021, 161: 103997.

[21] LAN Yong-ting, ZHONG Xian-ci, QUAN Gao-feng, LIN Ruo-cheng, ZHANG Ke-shi. Crystal anisotropy of AZ31 magnesium alloy under uniaxial tension and compression [J]. Transactions of Nonferrous Metals Society of China, 2015, 25(1): 249−260.

[22] LOU Y S, YOON J W. Anisotropic yield function based on stress invariants for BCC and FCC metals and its extension to ductile fracture criterion [J]. International Journal of Plasticity, 2018, 101: 125−155.

[23] COCKCROFT M, LATHAM D. Ductility and the workability of metals [J]. Journal Institute of Metals, 1968, 96: 33−39.

[24] BROZZO P, DELUCA B, RENDINA R. A new method for the prediction of formability in metal sheets [C]//Proceedings of the 7th Biennial Conference of IDDRG on Sheet Metal Forming and Formability. Amsterdam: Elsevier, 1972.

[25] OH S I, CHEN C C, KOBAYASHI S. Ductile fracture in axisymmetric extrusion and drawing. Part 2: Workability in extrusion and drawing [J]. Journal of Engineering for Industry, 1979, 101: 36−44.

[26] KO Y K, LEE J S, HUH H, KIM H K, PARK S H. Prediction of fracture in hub-hole expanding process using a new ductile fracture criterion [J]. Journal of Materials Processing Technology, 2007, 187/188: 358−362.

[27] XIAO X L, MU Z C, PAN H, LOU Y S. Effect of the Lode parameter in predicting shear cracking of 2024-T351 aluminum alloy Taylor rods [J]. International Journal of Impact Engineering, 2018, 120: 185−201.

[28] LOU Y S, ZHANG C, ZHANG S J, YOON J W. A general yield function with differential and anisotropic hardening for strength modelling under various stress states with non-associated flow rule [J]. International Journal of Plasticity, 2022, 158: 103414.

WE43 合金在不同应力状态下的本构关系及断裂行为表征

武鹏飞[1]，张 冲[1]，娄燕山[1]，陈 强[2]，宁海青[2]

1. 西安交通大学 机械工程学院，西安 710049；

2. 西南技术工程研究院，重庆 400039

摘 要：研究 WE43 合金在不同应力状态下的塑性和断裂行为。设计拉伸、压缩及剪切试样，并进行力学实验。采用数字图像相关技术对测试过程进行记录和处理。实验结果表明：WE43 合金具有低的拉压非对称性，其断裂机制属于韧性断裂。基于 Drucker 屈服函数，采用不同的硬化规律模拟单轴拉伸和压缩下的塑性变形行为。通过数值模拟得到应力状态和断裂应变。采用 Brozzo、Oh、Ko-Huh 和 DF2016 准则对韧性断裂行为进行数值预测，并与实验结果进行对比。结果表明：采用 Swift−Voce 硬化定律和 Drucker 屈服函数能合理模拟塑性变形。DF2016 断裂准则能准确预测合金在各种应力状态下的断裂行为。

关键词：稀土镁合金；塑性变形行为；应力状态效应；本构模型；韧性断裂预测

(Edited by Wei-ping CHEN)